Mini magnetospheres in the laboratory

Filipe Cruz
filipe.d.cruz@tecnico.ulisboa.pt

Instituto Superior Técnico, Lisboa, Portugal

May 2022

Abstract

The interaction between plasmas and magnetic obstacles often occur in astrophysical and space environments such as in ion-scale "mini magnetospheres". Such systems display a wide range of physical mechanisms and provide a unique environment for studying kinetic-scale plasma physics. In this Thesis, we present collisionless particle-in-cell (PIC) simulations of ion-scale magnetospheres that reproduce recent laboratory experiments performed on the Large Plasma Device (LAPD) at UCLA. In our PIC simulations, a driver plasma flows against a dipolar magnetic field that is embedded in a uniform magnetized background plasma. The simulations replicate the main magnetospheric structures observed in the experiments, namely the magnetopause and the plasma current distributions. We show the formation of a magnetic cavity and a magnetic compression and two main current structures in the dayside region. From multiple parameter scans, we show a reflection of the magnetic compression, bounded by the length of the driver plasma, and a higher separation of the main current structures for lower dipolar magnetic moments. Additionally, we develop an analytical model that characterizes the coupling between the driver and the magnetized background plasmas. The model is compared with the simulations, showing good agreement.

Keywords: mini magnetospheres, plasma coupling, PIC simulations, laboratory astrophysics, space physics

1. Introduction

A vast range of space and astrophysical scenarios are driven by the rapid expansion of plasmas through space. When these expanding plasmas encounter obstacles of magnetic nature, the resultant interaction leads to highly nonlinear and complex dynamics. In the solar system, the interaction between the plasma flow emmited by the Sun (*i.e.* the solar wind) and planetary-sized magnetic obstacles leads to the formation of magnetospheres [1].

The effective size of the magnetic obstacles is determined by the equilibrium position between the kinetic pressure of the solar wind and the magnetic pressure exerted by the planetary magnetic fields. The region of equilibrium, called the magnetopause, can be described using the pressure balance derived from magnetohydrodynamics (MHD)

$$n_d m_{i,d} v_0^2 = \frac{B^2}{8\pi} \tag{1}$$

where n_d is the density of the solar wind, v_0 is its flow velocity, $m_{i,d}$ is the mass of its ions, and B is the total magnetic field at the magnetopause. The total magnetic field can be written as $B = B_0 + B_{\rm dip}$, where B_0 is the plasma collective magnetic field and $B_{\rm dip} = M/L_0^3$ is the magnetic field of the obstacle, often well described by a dipolar profile of magnetic moment M. The plasma standoff distance L_0 between the center of the dipole and the magnetopause measures the effective size of the magnetic obstacle.

For planetary-sized magnetospheres, the obstacle size is typically tens of thousands of kilometers. However, magnetospheres with a few hundreds of kilometers are also observed in space environments such as the lunar surface. When the magnetic obstacle size is smaller or of the order of the ion kinetic scales of the plasma, the interaction with the solar wind results in ion-scale magnetospheres, or mini magnetospheres.

The study of mini magnetospheres in past years was mainly motivated by the observation of crustal magnetic anomalies on the lunar surface [2]. Although the Moon does not have a global magnetic field like Earth, it does have small localized regions of crustal magnetic field, of 10–100 nT over distances of 100–1000 km. As a result, when these regions of the lunar surface are exposed to the solar wind, mini magnetospheres can form.

Multiple experiments have been performed in laboratory settings that replicate the interaction be-

tween plasma flows and magnetic obstacles. In experimental studies, fast-moving plasmas are usually driven resorting to high-intensity lasers focused onto solid targets. By adding dipole field sources against the plasma flow, previous experiments studied the formation of lunar mini magnetospheres [3] and magnetosphere features [4]. Although these experiments achieved important breakthroughs, they were limited to 1D measurements.

Numerical simulations play a key role in interpreting and designing experiments. MHD and hybrid simulations attempted to explain the formation and characteristics of lunar mini magnetospheres and validate experimental and analytical models [5, 6]. However, these simulations do not resolve the electron scales and do not capture important kinetic effects. Particle-in-cell (PIC), were used to resolve the micro-physics of these systems and study its role in the formation of lunar mini magnetospheres [7] and collisionless shocks [8].

In this Thesis, we use PIC simulations of ion-scale magnetospheres driven by super-Alfvénic plasma flows to interpret the results of recent experiments [9] performed at the LArge Plasma Device (LAPD), a 20 m long, 1 m diameter, cylindrical facility for general-purpose research in plasma physics at the University of California, Los Angeles. In these experiments, fast collisionless driver plasma flows generated by high-repetition-rate lasers were collided with a magnetized background plasma and with a dipolar magnetic field obstacle, leading to the formation of ion-scale magnetospheres. Using motorized probes, measurements of the magnetic field allowed characterization of 2D magnetic field and current density structures.

In Section 2, we describe the coupling, *i.e.* the energy and momentum transfer efficiency, between the driver and background plasmas, to understand the experiments at early times. We describe the evolution of the plasmas and derive analytical expressions for the coupling. In Section 3, we present PIC simulations of ion-scale magnetospheres, and show the main characteristics of the system, namely a reflection of the background magnetic compression and the formation of two dayside current structures. In Section 4, resorting to simulations with a wide range of parameters, we show that the length of the driver bonds the reflection of the compression, and that lower dipolar magnetic moments lead to a larger separation of the two currents.

2. Driver-background plasma coupling

In the LAPD experiments, a mini magnetosphere was produced in a laboratory by colliding a driver plasma against a dipole embedded in a magnetized background plasma. In this setup, the driver interacts with the background before suffering significant effects by the magnetic field of the dipole. During this stage, the coupling between the plasmas determines the system evolution. To fully comprehend the dynamics of the experiments, we first need to understand the interaction between the driver and the background plasmas.

2.1. Setup of the simulations

We have performed multiple 1D simulations with OSIRIS, a massively parallel and fully relativistic PIC code [10, 11], of an unmagnetized plasma flowing against a magnetized background plasma. With PIC simulations, we can accurately resolve the plasma kinetic scales of these systems.

The 1D simulations consist in a 25 d_i length region, with open boundary conditions at $x = -5\ d_i$ and $x = 20\ d_i$, where $d_i = c/\omega_{pi} = \sqrt{m_{i,0}c/4\pi n_0 e^2}$ is the ion skin depth of the background plasma, c is the speed of light in vacuum, ω_{pi} is the ion plasma frequency, e is the electron charge, and $m_{i,0}$ and n_0 are the ion mass and the density of the background plasma, respectively. Since the most relevant dynamics of the system occurs at the ion kinetic scales, the spatial scales were normalized to d_i, and the time scales to the ion cyclotron frequency of the background plasma $\omega_{ci}^{-1} = m_{i,0}c/eB_0$, where B_0 is the background magnetic field. The simulations consider 200 particles per cell per species. To resolve the dynamics of the electron kinetic scales, we used 10 grid cells per electron skin depth, $d_e = d_i\sqrt{m_e/m_{i,0}}$.

We consider an idealized and simplified driver plasma in the simulations, compared to the experimental laser-produced plasma. The driver flows toward the positive x direction with fluid velocity $\mathbf{v_0} = v_0\hat{\mathbf{x}}$, has a uniform density n_d, and a length $L_x = 5\ d_i$. The driver is initially located between $x = -5\ d_i$ and $x = 0$ and it is composed by ions with mass $m_{i,d}$ and electrons. Equivalently, the background plasma has density n_0 and length of 20 d_i. It is located between $x = 0$ and $x = 20\ d_i$ and it is composed ions with mass $m_{i,0}$ and electrons. Unlike the driver, the background plasma is magnetized by an internal and uniform magnetic field $\mathbf{B_0} = B_0\hat{\mathbf{z}}$. The magnitude of B_0 is calculated from the Alfvénic Mach number, defined as $M_A \equiv v_0/v_A = v_0\sqrt{4\pi n_0 m_{i,0}}/B_0$, where v_A is the Alfvén velocity. All the ions have charge $q_i = e$ and the electrons have mass m_e.

The simulations consider cold plasmas, reduced ion mass ratios $m_{i,0}/m_e = 100$, and faster fluid velocities $v_0 = 0.1\ c$ than expected in experiments and most astrophysical scenarios. These approximations are done to reduce the required computational resources necessary to perform the simulations, allow extended scans over different parameters, and simplify our analysis. The chosen ion-to-

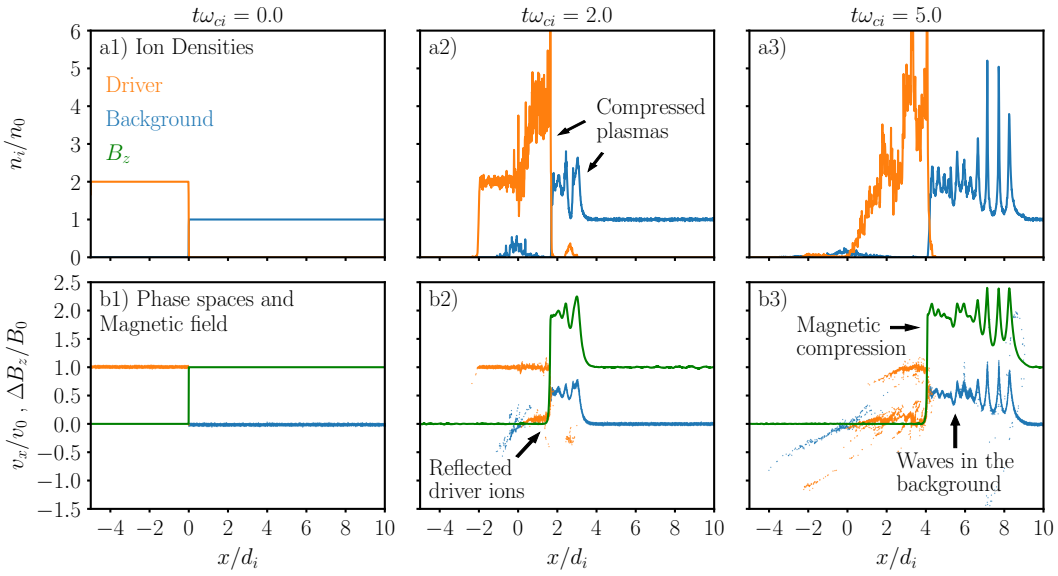

Figure 1: a) Ion densities n_i and b) x component of the ion velocities v_x, for the driver (orange) and background (blue) plasmas. The green line shows the magnetic field B_z. Columns 1-3 correspond to three different time steps. The simulation considers $n_d = 2\ n_0$, $m_{i,d} = m_{i,0}$, and $M_A = 1.5$.

electron mass ratio in the simulations is high enough to ensure sufficient separation between electron and ion spatial and temporal scales. In these systems, the thermal effects are typically negligible and do not affect the main results. We considered electron thermal velocities $v_{the} = 0.1\ v_0$ for both the plasmas, and that the ions and electrons are initially in thermal equilibrium.

2.2. Basic system dynamics

Figure 1 illustrates the basic temporal evolution of the system, and shows the ion densities n_i of the driver and background plasmas, the ion phase spaces, and the magnetic field B_z, for three different time steps. The initial setup of the simulations is represented in Figures 1 a1) and b1). This simulation considers $M_A = 1.5$, $n_d/n_0 = 2.0$ and $m_{i,d} = m_{d,0}$.

As shown in Figures 1 a2) and a3), the driver flows to the right and drives the background plasma and magnetic field with it, leading to a relocation of the interface between the two plasmas and creating high density regions. During this process, the driver plasma is mostly confined upstream, while the background plasma downstream.

Due to the large mass discrepancies between the ions and electrons, the driver electrons near the background are highly magnetized while the driver ions are effectively unmagnetized. This resulting space charge separation creates the electric field E that deflect the driver ions and provides an $E \times B$ drift for the driver electrons. The electrons generate a diamagnetic current that produces an opposing magnetic field to the background magnetic field, leading to a magnetic cavity, as we observe in Figures 1 b1-3). As the driver particles flow with velocity v_0 against the background, they interact with this electric field, and end up reflected back upstream with velocity v_1. As this happens, the bulk of the driver travels to the right through the region initially occupied by the background plasma.

The energy and momentum lost by the driver plasma during this process are transferred to the background. The initially stationary background ions are accelerated and the magnetic field is compressed. Multiple waves and instabilities are excited in the background region, leading to the oscillations observed in Figure 1.

Figure 1 also shows that the magnetic field and density profiles of the system are not constant. However, some averaged quantities of the system do not change significantly over time. We can, therefore, consider that system achieves a quasi-stationary regime that can be represented by average properties. In Section 2.7, we show that these properties can be calculated by analytical expressions and can describe the coupling between the plasmas.

2.3. Magnetic and current density diagnostics

To comprehend the dynamics of these systems, it is important to investigate the evolution of B_z, since it determines the motion of the particles. From Ampère's law, the y component of the current density is given by $J_y \approx -(c/4\pi) \cdot \partial B_z/\partial x$, and so, we can use J_y to investigate the changes in the magnetic field.

To illustrate these two important quantities, we

show in Figure 2 the temporal evolution of a) the variation of the magnetic $\Delta B_z = B_z - B_{z,\mathrm{ini}}$, where $B_{z,\mathrm{ini}}$ is the initial magnetic field, and b) the current density J_y. These diagnostics are shown for $n_d/n_0 = 2$, $M_A = 1.5$ and $m_{i,d} = m_{i,0}$.

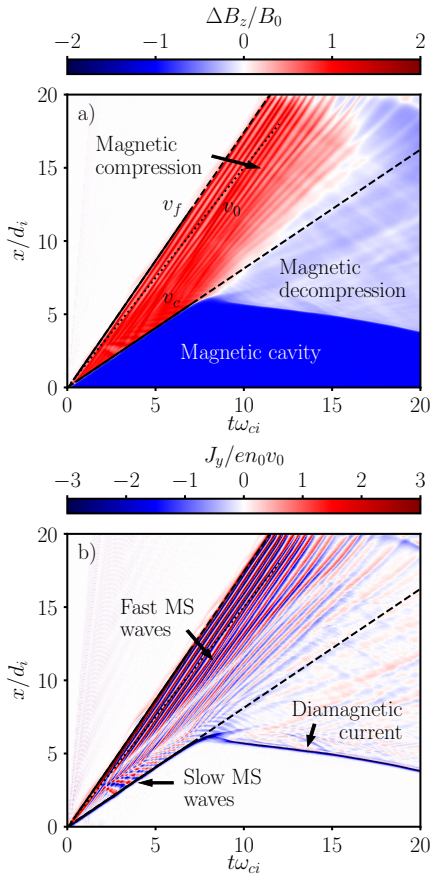

Figure 2: Temporal evolution of a) the variation of the magnetic field B_z and b) current density J_y for $n_d/n_0 = 2$, $M_A = 1.5$ and $m_{i,d} = m_{i,0}$. The dotted line has a slope v_0, and the slopes of the solid and dashed lines are given by the coupling velocity v_c and the front velocity v_f, respectively.

While the driver flows against the background, it expels the magnetic field, creating the magnetic cavity that can be observed in Figure 2 a). This magnetic cavity expands over time and the velocity at which it travels through the background is designated by coupling velocity v_c.

As observed in Figure 1, the driver ions flow against the background region and get reflected by an electric field. As a result, the amount of driver ions traveling with velocity v_0 decreases over time. After all the driver ions ended up reflected, the magnetic cavity will be reflected as well.

Besides the formation of the magnetic cavity, we also observe in Figure 2 a) the magnetic compression downstream, where the background is located. The average of the compressed magnetic field does not change significantly over time in the simulations, for the main interaction of the system. The ratio of averaged compressed to initial magnetic field is designated by compression ratio α. The velocity at which the magnetic compression travels through the unperturbed background is designated by front velocity v_f.

Figure 2 b) shows the current density for this simulation. The jump on the magnetic field from the magnetic cavity to the magnetized plasma is described by the diamagnetic current. In the background region, we also observe multiple current structures associated with the slow and fast magnetosonic waves.

2.4. Simplified model for the system

If the plasmas are long enough, the system reaches a quasi-stationary regime where the main averaged parameters of the system do not change over time. Under this assumption, the system can be separated into different regions with similar properties, and can be modeled by the configuration shown in Figure 3. Here, we neglect thermal effects, instabilities, and electron pressure effects. This simplifications should not affect the description of the coupling for $M_A \sim 1$, cold plasmas, and the uniform densities considered in this Thesis.

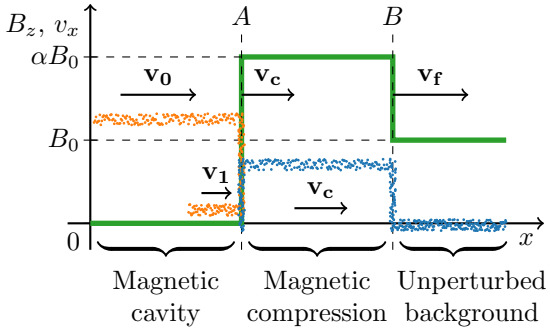

Figure 3: Simplified model of the interaction between the flowing driver (orange) with the background (blue) and magnetic field profile (green). The dots illustrate the plasma particles velocities. This model considers three regions: the magnetic cavity, the magnetic compression, and the unperturbed background regions. These regions are separated by the discontinuities A and B.

The model considers three regions with different characteristics. The first refers to the magnetic cavity, where $B_z \approx 0$. The driver plasma is located in this upstream region, and the ion motion of the driver can be described by two ion flows with velocity $\mathbf{v_0}$ and $\mathbf{v_1}$. The second region is located in the magnetic compression, and the average magnetic field is αB_0. In this region, the background ions accelerated by the driver plasma have average

velocity $\mathbf{v_c}$. The third region, is the background that remains unperturbed. Here, the magnetic field is B_0 and the background ions have no flow velocity.

These regions are separated by two discontinuities labeled A and B, where the properties change abruptly, and move through the simulation box with velocity $\mathbf{v_c}$ and $\mathbf{v_f}$, respectively. From the upstream to the downstream side of the discontinuities, the mass, momentum, and energy flows, must be conserved. These conservation laws lead to the Rankine-Hugoniot (R-H) jump conditions, which relate the parameters of the each side of the discontinuities.

2.5. Physics at the boundaries

To relate the parameters of each region of Figure 3, we first look at the conservation equations for a single discontinuity. We define regions 1 and 2 as the upstream and downstream sides of this discontinuity, and that each side is described by a different set of parameters.

By integrating the MHD and Maxwell's equations over the discontinuity, we can relate the plasma quantities of both sides. Using the previous Equations for A and B, we can relate α, v_c, and v_f with

$$\alpha \equiv \frac{B_0'}{B_0} = \frac{n_0'}{n_0} = \frac{v_f}{v_f - v_c} \tag{2}$$

$$2n_d m_{i,d}(v_0 - v_c)^2 = \frac{(\alpha B_0)^2}{8\pi} \tag{3}$$

where B_0' and n_0' represent the average magnetic field and density of the compressed background.

2.6. Energy conservation of the system

To complement the previous equations, we now consider the energy conservation of the system. Considering ΔE_d, ΔE_0, ΔE_mag and ΔE_ele as the energy variations of the system associated with the driver plasma, the background plasma, the magnetic field, and the electric field, respectively, over a time Δt, we must have from energy conservation

$$E_\mathrm{d} + \Delta E_0 + \Delta E_\mathrm{mag} + \Delta E_\mathrm{ele} = 0 \tag{4}$$

Because we neglect thermal effects and $m_e \ll m_i$, the plasmas energies are mostly transferred by the ions instead of electrons. If we consider the model in Figure 3 and represent the energy variations in average quantities, then the expressions for the each energy variation term, for an area A_T transverse to the flow and a time Δt are

$$\Delta E_\mathrm{d} = -2n_d m_{i,d}(v_0 - v_c)^2 v_c A_T \Delta t \tag{5}$$

$$\Delta E_0 = \frac{1}{2} m_{i,0} v_c^2 n_0 v_f A_T \Delta t \tag{6}$$

$$\Delta E_\mathrm{mag} = \frac{B_0^2}{8\pi}\left[\alpha^2(v_f - v_c) - v_f\right] A_T \Delta t \tag{7}$$

Since $v \ll c$, then $\Delta E_\mathrm{ele} \ll \Delta E_\mathrm{mag}$, and so, the electric energy can be neglected.

2.7. Coupling parameters

Equations (2) to (7) relate the coupling parameters α, v_c, and v_f with the initial parameters of the system. By defining R_n as

$$R_n = \frac{1}{2}\left(\frac{n_0}{n_d}\frac{m_{i,0}}{m_{i,d}}\right)^{\frac{1}{2}} \tag{8}$$

we can show that the coupling parameters are given by

$$\alpha = \frac{1 + M_A}{1 + R_n} \tag{9}$$

$$\frac{v_c}{v_0} = \frac{1}{M_A}\frac{M_A - R_n}{1 + R_n} \tag{10}$$

$$\frac{v_f}{v_0} = \frac{1}{M_A}\frac{M_A + 1}{1 + R_n} \tag{11}$$

These analytical expressions depend only on the initial parameters and are easily calculated from the magnetic data. To validate Equations (9) to (11), we performed multiple PIC simulations with different Mach numbers M_A and driver densities n_d, with $m_{i,d} = m_{i,0}$, and measured the coupling parameters for each one. Figure 4 shows the obtained measurements alongside Equations (9) to (11).

Figure 4 shows that the results of the simulations are consistent with the derived equations, for $M_A \sim 1$. As expected, Figures 4 a) and b) show that v_c and α increase with n_d and M_A. We also observe that some simulations had negative coupling velocities. In these cases, the driver is not strong enough to push the background, and a background magnetic decompression occurs instead ($\alpha < 1$).

In Figure 4 c), we see that the front velocity increases with n_d and decreases with M_A. Although, Equation (11) is consistent with the simulations results, we start observing a more meaningful discrepancy in v_f than in v_c and α, in particular for low and high Mach numbers. For low Mach numbers $M_A < 1$, these differences are associated with the difficulty in measuring v_f in the simulations, due to the low compression ratios. For high Mach numbers $M_A > 1$, Equation (6) underestimates the energy of the background since it does not consider instabilities, leading to errors in the derived equations.

With Equations (9) to (11) we are now able to describe the coupling between the plasmas in the early stages of the experiments.

3. PIC simulations of mini magnetospheres

After understanding the interaction between a driver plasma flowing against a magnetized plasma, we can now study how the system changes when a dipole is introduced. These configuration leads to

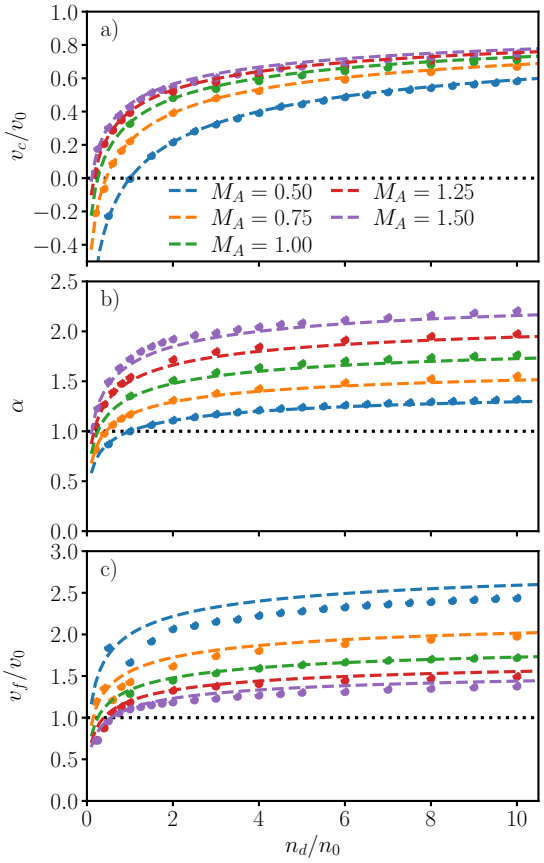

Figure 4: Comparison between the coupling parameters measured in the simulations for a) v_c/v_0 with Equation (10), b) α with Equation (9), and c) v_f/v_0 with Equation (11), for multiple M_A and n_d/n_0 values. These simulations considered $m_{i,d} = m_{i,0}$. The simulation results are represented by the dots and the analytical expressions by dashed lines.

a mini magnetosphere, as observed in the recent LAPD experiments [9].

3.1. Setup of the simulations

Motivated by the results of the LAPD experiments, we performed 2D PIC simulations with OSIRIS. The numerical simulations presented in this work stem from a simplified description of the experimental setup, represented in Figure 5. In these simulations, a driver plasma moves against a background plasma permeated by a uniform magnetic field $\mathbf{B_0}$ and a dipolar magnetic field $\mathbf{B_{dip}}$. $\mathbf{B_0}$ and $\mathbf{B_{dip}}$ are oriented along the $\hat{\mathbf{z}}$ and are transverse to the driver plasma flow. The simulation box is a 12 d_i × 12 d_i area with open and periodic boundary conditions in the x and y directions, respectively. The flow is in the x direction and the size of the simulation domain in the y direction is large enough to avoid re-circulation of the particles. The simulations considered 25 particles per cell per species. To resolve the dynamics of the electron kinetic scales, we used 10 grid cells per electron skin depth d_e in both x and y directions.

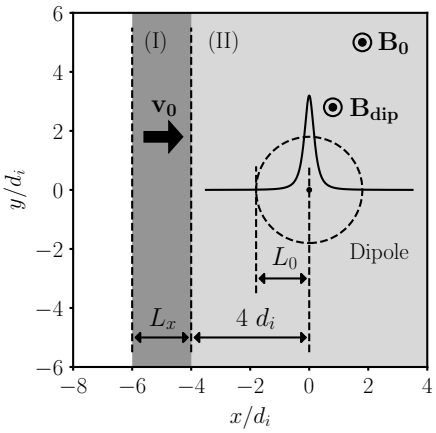

Figure 5: Schematic illustration of the initial setup of the 2D PIC simulations performed. The system considers a vacuum region at the left, a driver plasma (I), and a magnetized background plasma (II). A dipole is included at the center of the background region.

The driver plasma, shown in region I in Figure 5, represents ideally the experimental driver plasma. We assume that this driver has a length L_x that is typically 2 d_i, and a width L_y that is typically infinite. It has a constant density n_d, and it is initialized moving to the right side with initial flow velocity v_0. The driver is composed of an electron species and a single ion species, with ion mass $m_{i,d}$.

The background plasma is represented in region II. It is an 8 d_i length and infinite width plasma and it has uniform density n_0. The initial interface between the driver and background plasma is located at $x_B = -4$ d_i. Like the driver plasma, it has an electron species and a single ion species, of mass $m_{i,0}$. The background plasma is magnetized with an internal uniform magnetic field $\mathbf{B_0} = B_0\hat{\mathbf{z}}$, and its magnitude is defined such that the Alfvénic Mach number of the flow matches the peak experimental value $M_A = 1.5$, where v_A is the Alfvén velocity.

A dipolar magnetic field is externally imposed in our simulations. The dipole is centered at $(x, y) = (0, 0)$ and its associated magnetic field is $\mathbf{B_{dip}} = B_{\rm dip}\hat{\mathbf{z}}$, with $B_{\rm dip} = M/r^3$, where M is the dipolar magnetic moment, $r = \sqrt{x^2 + y^2 + \delta^2}$ is the distance to the dipole's origin and $\delta = 0.25$ d_i is a regularization parameter. For most simulations, M was chosen such that the expected standoff, obtained from Equation (1), is similar to the experimental value $L_0 = 1.8$ d_i [9].

The physical parameters of the simulations (e.g. M_A, L_0/d_i) were adjusted to be similar to the

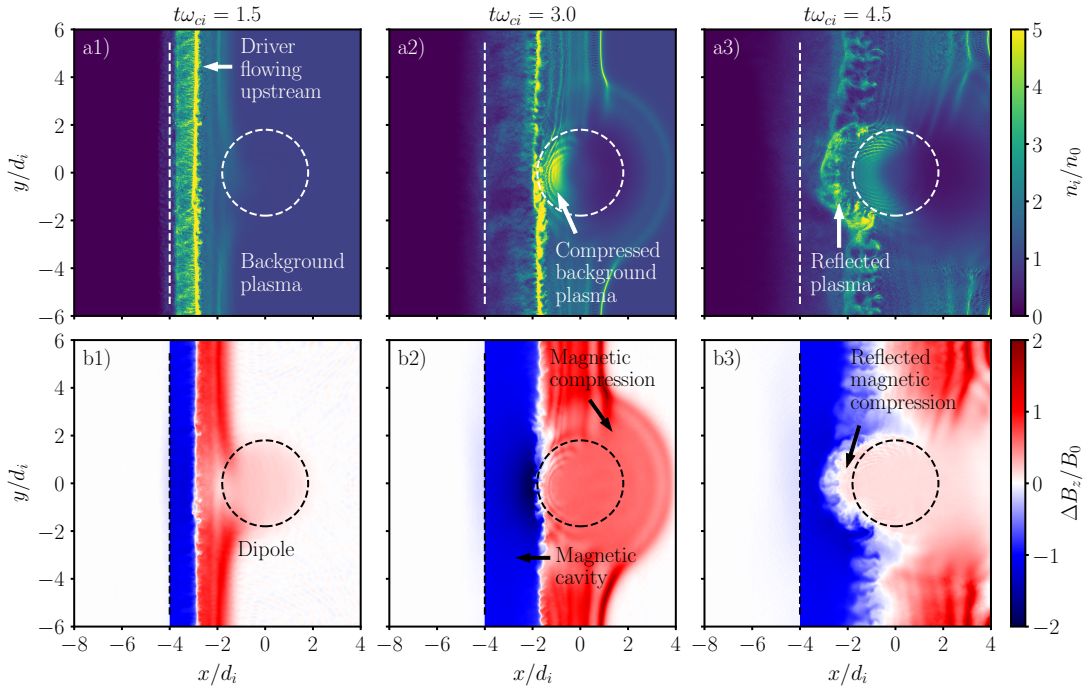

Figure 6: Spatiotemporal evolution of a) the total ion density and b) the variation of the z component of the magnetic field in the standard simulation. Columns 1-3 correspond to three different times. The vertical and circular dashed lines mark the initial border between the driver and background plasma and the dipolar obstacle with radius L_0, respectively.

LAPD experiments, whereas other parameters (e.g. m_i/m_e, v_0) were chosen to make simulations computationally feasible. We again considered a reduced mass ratio $m_i/m_e = 100$, a flow velocity $v_0/c = 0.1$, and cold plasmas. We have assumed that ions and electrons are initially in thermal equilibrium. These simulations considered $m_{i,d} = m_{i,0}$.

3.2. Evolution and formation of a mini magnetosphere

To identify the main magnetospheric and kinetic-scale structures that arise from the initial configuration, a standard simulation was performed with a driver length $L_x = 2\ d_i$ and density $n_d = 2\ n_0$. Figures 6 a1-3) represent the total ion density $n_i = n_{i,d} + n_{i,0}$, for three different times, and Figures 6 b1–3) show the variation of the z component of the magnetic field, from its initial value, $\Delta B_z = B_z - B_{z,\text{initial}}$.

In Figure 6 a1), we see the total ion density for an early time ($t\omega_{ci} = 1.5$). Given the small distance propagated by the driver plasma at this time, the dipolar magnetic field does not significantly affect the interaction between the plasmas. We can express the early system as a driver flowing against a uniform magnetized background plasma, as described in Section 2. In Figure 6 b1), we observe the compressed magnetic field downstream, and the magnetic cavity upstream.

In Figures 6 a2) and b2), we start to observe the effects of the dipolar magnetic field for a later time ($t\omega_{ci} = 3.0$). As the magnetic pressure exerted against the plasmas increases, a region of compressed background plasma forms in front of the dipole. After the interaction background-dipole, the magnetic field pressure becomes large enough to counterbalance the kinetic pressure of the driver, reflecting it upstream, as seen in Figure 6 a3) for a subsequent time ($t\omega_{ci} = 4.5$). After the reflection, there is no longer a plasma flow pushing/holding the magnetic compression, and as a result, the region near the dipole quickly decompresses.

3.3. Magnetic field and current density synthetic diagnostics

To compare the numerical results with the experimental data [9], synthetic diagnostics were obtained for the simulations. In Figure 7, ΔB_z and J_y measured at $y = 0$ are plotted for the standard simulation.

The main features of Figure 7 are consistent with the experimental results [9]. In the magnetic field plot of Figure 7 a), both the upstream magnetic cavity and the downstream magnetic compression are present. Until $t\omega_{ci} \approx 1.5$, the system behaves approximately as a driver piston moving against a uniform magnetized plasma.

The driver experiences increasingly higher mag-

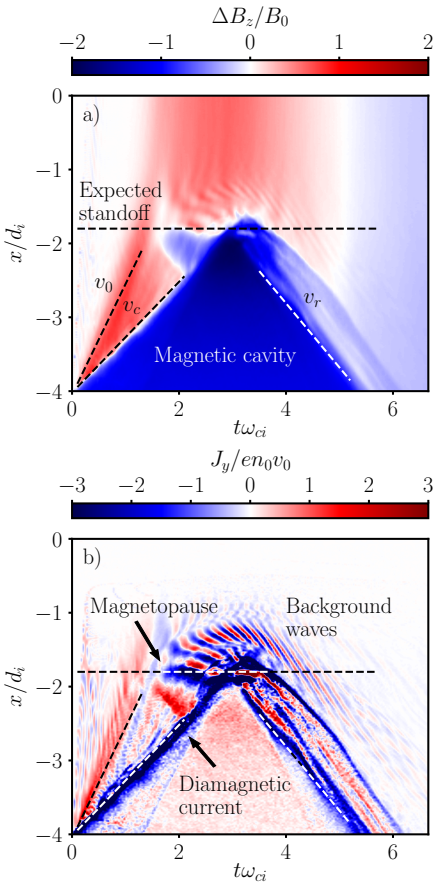

Figure 7: Temporal evolution of a) ΔB_z and b) J_y at $y = 0$ for the standard simulation. The dashed lines have slopes that match v_0, v_c, and the reflection velocity v_r.

netic fields until the magnetic pressure is enough to reflect the driver near the expected standoff $x_0 = -L_0$, at $t\omega_{ci} \approx 3$. The magnetic cavity and magnetic compression are also reflected, and the boundary between these two regions travels with a velocity v_r after reflection. The background magnetic decompression is seen after $t\omega_{ci} = 5$.

In the current density plot of Figure 7 b), we can observe the diamagnetic current that identifies the leading edge of the magnetic cavity. During the driver reflection, this current branches into multiple components due to the multi-stream velocity distributions developed in the plasmas. We can also verify that this structure is reflected near $x_0 = -L_0$. Between $t\omega_{ci} \approx 2$ and $t\omega_{ci} \approx 3$, a second current structure is present in the background region. It is associated with the two magnetopauses of the system: the first corresponds to the interaction background-dipole and the second to the driver-dipole.

4. Parameter scans

To find the parameters that best reproduced the experimental results and to understand their role in the system, we performed multiple parameter scans. In this Section, we present the main results for driver length and dipolar magnetic moment scans.

4.1. Driver length

Simulations C1 to C3 were performed with varying driver length L_x. In Figure 8, we show ΔB_z and J_y at $y = 0$, for $L_x = 1\ d_i$ (C1), $L_x = 4\ d_i$ (C2) and for an infinite driver (C3). For these simulations, the properties of the background plasma and the width of the driver L_y were kept unchanged. The density of the driver was $n_d = 2\ n_0$.

In Figures 8 a1) and b1), we see the magnetic field and current density plots for the short driver length $L_x = 1\ d_i$. We observe most of the features of Figure 7, namely the reflection of the magnetic compression and the diamagnetic and magnetopause currents. For this length, the driver never fully interacts with the dipole. The closest that the diamagnetic current gets to the dipole is $x_r \approx -3.0\ d_i$, *i.e.*, much farther than the expected standoff $x_0 = -1.8\ d_i$. To replicate the experimental results we must ensure that the driver is sufficiently long such that $x_r > x_0$.

In the simulation with $L_x = 4\ d_i$, represented in Figures 8 a2) and b2), we observe once again the main features identified in Figure 7. Unlike the $L_x = 1\ d_i$ case, the driver is long enough to end up reflected by the dipole. We observe that the diamagnetic current reaches the expected standoff and has enough plasma to maintain it near the dipole for a time period ($t\omega_{ci} \approx 3$ to $t\omega_{ci} \approx 5$) longer than the $2\ d_i$ case. As a result, the background magnetic decompression is delayed for long drivers. However, because the full driver reflection also occurs later, long drivers result in short-lived reflections of the magnetic compression.

In Figures 8 a3) and b3), we show the results for a driver with infinite length ($L_x = +\infty$). Until $t\omega_{ci} = 3$, the features observed are very similar to Figure 7. After this time, the magnetic and the driver kinetic pressures balance each other near x_0, so the diamagnetic current remains stationary. Because the driver holds near the dipole, the decompression in the background is considerably delayed.

Given the results shown in Figure 8, we chose a driver length of $2\ d_i$ to reproduce the experimental results. This driven length is large enough to ensure that the driver arrives at the dipole and small enough to observe a significant reflection of the magnetic compression.

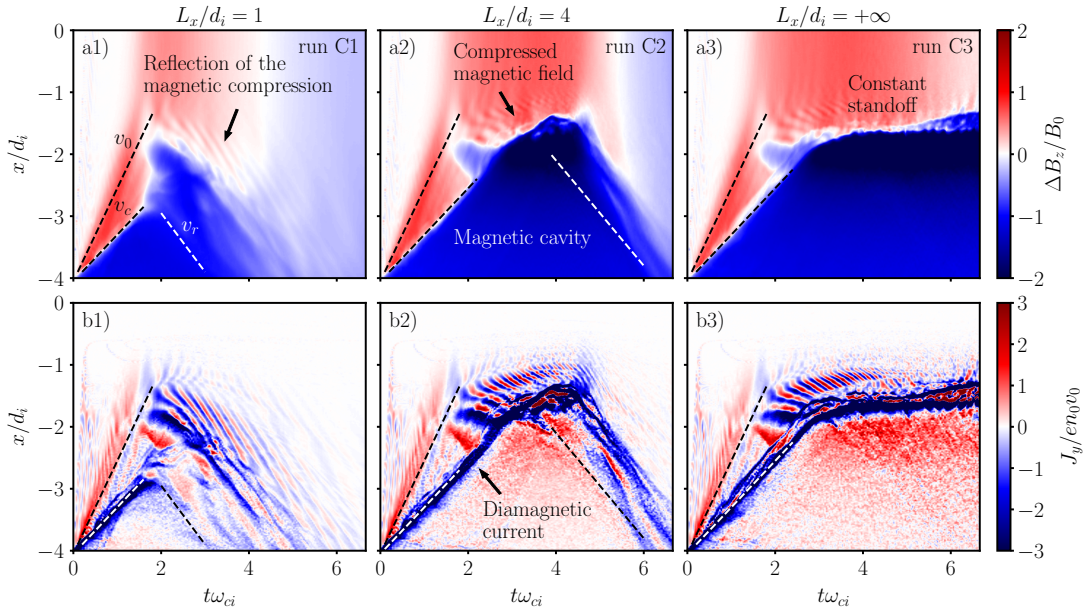

Figure 8: Temporal evolution of ΔB_z and J_y at $y = 0$, for driver lengths of a) 1 d_i, b) 4 d_i and for c) an infinite driver length.

4.2. Magnetic moment of the dipole

We performed simulations with a 2 d_i long driver with density $n_d = 2\ n_0$ for three different magnetic moments. Considering the magnetic moment that results in the expected standoff $L_0 = 1.8\ d_i$ as M_0 (standard simulation), simulations with the magnetic moments 2 M_0 (E1) and $M_0/2$ (E3) were also performed. Figure 9 shows the synthetic diagnostics at $y = 0$ for the three simulations.

Figures 9 a1) and b1) show the results for the highest magnetic moment $M = 2\ M_0$. We see that the current structures associated with the magnetopause are less evident than for the lower magnetic moments, as they are formed farther from the dipole. Figures 9 a2) and b2) correspond to Figure 7, and as previously mentioned, there are two main observable current structures. The first one is associated to the diamagnetic current, which is reflected around $t\omega_{ci} \approx 3$ near $x_0 = -1.8\ d_i$. The second occurs between $t\omega_{ci} \approx 2$ and $t\omega_{ci} \approx 3$, it is located in the background and it is associated with the magnetopause.

In Figures 9 a3) and b3), we show the results for the half magnetic moment $M = M_0/2$. In this case, the magnetic pressure exerted by the dipole is lower, leading to a smaller L_0, and consequently, the diamagnetic current is closer to the dipole than in Figures 9 b1) and b2). The main changes, however, occur in the magnetopause current. Unlike what we observe for the other magnetic moments, the magnetopause current lasts for a longer time (until $t\omega_{ci} \approx 4$), and it is first associated with the background-dipole interaction, and then with the driver-dipole. This current is also more separated from the diamagnetic current for the lower magnetic moments.

5. Conclusions

In the interaction between an unmagnetized driver plasma flowing against a uniform magnetized background plasma, the initial driver flow expels the magnetic field in the upstream region, leading to a magnetic cavity, and compresses the background magnetic field. We have studied this interaction analytically and numerically, resorting to PIC simulations. For Alfvénic Mach numbers close to unity, we calculated the velocities of the magnetic cavity and magnetic compression, and the magnetic field compression ratio. For higher Mach numbers, instabilities are triggered during the interaction, and must be considered for the system's energy partition.

When a magnetic dipole is placed in front of the flow, the driver travels through the background until the magnetic field pressure is large enough to counterbalance the driver plasma pressure, leading to the formation of mini magnetospheres. In this work, we explored the behaviour of these systems under a wide range of parameters with PIC simulations. We observed a fast decompression of the background magnetic field. If the background decompression occurs after the total reflection of the driver, then we observe the reflection of the magnetic compression. From parameter scans, we showed that, in order to see this feature, the driver needs to be short enough to anticipate the driver reflection relative to the decompression but long

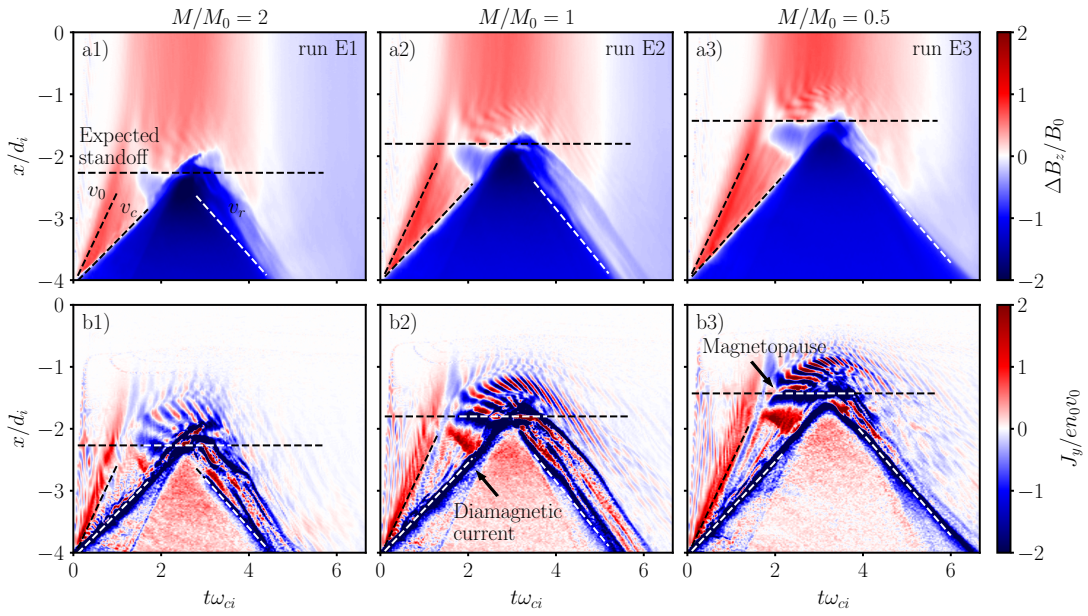

Figure 9: Temporal evolution of ΔB_z and J_y at $y = 0$, for three different magnetic moments. The magnetic moments M considered were a) $M = 2\ M_0$, b) $M = M_0$ and c) $M = M_0/2$.

enough to ensure that it can stand close to the dipole.

The interaction of the plasmas with the dipole results in two magnetopauses. The first occurs due to the background-dipole interaction and the second from the driver-dipole. For lower magnetic moments, the magnetopause current is more clearly identified and easier to separate it from the diamagnetic current than for lower moments, consistently with the experiments.

In conclusion, we have successfully reproduced results of recent LAPD experiments, validating the platform to study mini magnetospheres in the laboratory. From parameter scans we determined how the main properties of the system change with the parameters and identified conditions for the magnetospheric features observed in the experiments. With both numerical and analytical studies, we derived equations that describe the driver-background coupling. This work is an important step for upcoming experiments at the LAPD because it allows us to find the parameters that ensure the observation of laboratory mini magnetospheres.

Acknowledgements

I acknowledge Dr. Fábio Cruz, Prof. Luís Silva, and Dr. Derek Schaeffer for the guidance through this project. I also acknowledge the support of the European Research Council, FCT, the NSF/DOE Partnership in Basic Plasma Science and Engineering, and PRACE for awarding access to MareNostrum. The simulations were performed at the IST cluster and MareNostrum.

References

[1] C. Russell *Annual Review of Earth and Planetary Sciences*, vol. 19, no. 1, pp. 169–182, 1991.

[2] R. P. Lin *et al. Science*, vol. 281, no. 5382, pp. 1480–1484, 1998.

[3] R. A. Bamford *et al. Physical Review Letters*, vol. 109, no. 8, p. 081101, 2012.

[4] P. Brady *et al. Physics of Plasmas*, vol. 16, no. 4, p. 043112, 2009.

[5] E. M. Harnett and R. Winglee *Journal of Geophysical Research: Space Physics*, vol. 105, no. A11, pp. 24997–25007, 2000.

[6] L. Gargaté *et al. Plasma Physics and Controlled Fusion*, vol. 50, no. 7, pp. 1–12, 2008.

[7] M. I. Zimmerman, W. M. Farrell, and A. R. Poppe *Journal of Geophysical Research: Planets*, vol. 120, no. 11, pp. 1893–1903, 2015.

[8] F. Cruz *et al. Physics of Plasmas*, vol. 24, no. 2, p. 022901, 2017.

[9] D. B. Schaeffer *et al. Physics of Plasmas*, vol. 29, no. 4, p. 042901, 2022.

[10] R. A. Fonseca *et al.* in *Lecture Notes in Computer Science*, vol. 2331 LNCS, pp. 342–351, Springer Verlag, 2002.

[11] R. A. Fonseca *et al. Plasma Physics and Controlled Fusion*, vol. 55, no. 12, p. 124011, 2013.